Received: 30 March 2020 | Revised: 21 May 2020 | Accepted: 23 May 2020

DOI: 10.1002/mrm.28376

FULL PAPER

Magnetic Resonance in Medicine

Fast chemical exchange saturation transfer imaging based on PROPELLER acquisition and deep neural network reconstruction

Chenlu Guo[1] | **Jian Wu**[1] | **Jens T. Rosenberg**[2] | **Tangi Roussel**[2] | **Shuhui Cai**[1] | **Congbo Cai**[1]

[1]Department of Electronic Science, Fujian Provincial Key Laboratory of Plasma and Magnetic Resonance, Xiamen University, Xiamen, China

[2]The National High Magnetic Field Laboratory, Florida State University, Tallahassee, FL, USA

Correspondence
Shuhui Cai, Department of Electronic Science, Fujian Provincial Key Laboratory of Plasma and Magnetic Resonance, Xiamen University, Xiamen 361005, China.
Email: shcai@xmu.edu.cn

Funding information
National Natural Science Foundation of China, Grant/Award Number: 11775184 and 81671674; National Science Foundation, Grant/Award Number: DMR-1644779; State of Florida

Purpose: To develop a method for fast chemical exchange saturation transfer (CEST) imaging.

Methods: The periodically rotated overlapping parallel lines enhanced reconstruction (PROPELLER) sampling scheme was introduced to shorten the acquisition time. Deep neural network was employed to reconstruct CEST contrast images. Numerical simulation and experiments on a creatine phantom, hen egg, and in vivo tumor rat brain were performed to test the feasibility of this method.

Results: The results from numerical simulation and experiments show that there is no significant difference between reference images and CEST-PROPELLER reconstructed images under an acceleration factor of 8.

Conclusion: Although the deep neural network is trained entirely on synthesized data, it works well on reconstructing experimental data. The proof of concept study demonstrates that the combination of the PROPELLER sampling scheme and the deep neural network enables considerable acceleration of saturated image acquisition and may find applications in CEST MRI.

KEYWORDS
chemical exchange saturation transfer, deep neural network, PROPELLER

1 | INTRODUCTION

Chemical exchange saturation transfer (CEST) provides a highly sensitive detection mechanism for MRI.[1-5] CEST MRI can reveal physiological and pathological characteristics of organism tissues indirectly by quantitatively characterizing chemical exchange between selectively saturated labile protons of low-concentration (in millimolar to nanomolar range) solutes and water.[6,7] Its sensitivity has been successfully demonstrated both in vitro[8,9] and in vivo.[10,11] On account of its unique mechanism, CEST MRI plays an increasingly important role in the field of medical imaging. For example, some diseases can be diagnosed through detecting pathological and chemical changes by CEST MRI, such as cranial nervous system diseases,[12,13] cerebral ischemia,[14-16] and cancer.[17-19]

However, the application of CEST MRI is evidently limited by the long saturation duration to maintain the process

of saturation labeling, and the special sampling requirement of multiple saturated images at different saturation frequency offsets.[20,21] For example, the saturation duration should be longer than the T_1 of the bulk water protons to prevent loss of saturation.[22] Additionally, it is necessary to acquire enough saturated images in a wide range of saturation frequency offsets to accurately capture various effects in the Z-spectrum.[23,24] Usually, CEST MRI sequences are composed of a long-duration off-resonance RF irradiation module and a fast image readout module such as fast spin echo (FSE) or echo planar imaging (EPI).[25-28] Compared with FSE, EPI can significantly reduce scan time, but it is vulnerable to field inhomogeneity and chemical shift effects, and generates signal voids or distortion at the tissue-air interface, which might disturb the accuracy of the measured results.[29]

In this study, we introduce a sampling pattern based on periodically rotated overlapping parallel lines enhanced reconstruction (PROPELLER)[30] into CEST MRI to dramatically accelerate CEST imaging (dubbed as CEST-PROPELLER). Similar to the compressed sensing method in CEST imaging that can reduce the scan time by randomly undersampling k-space data,[31] the CEST-PROPELLER sampling scheme is used to acquire only several lines from the k-space center per saturated image. Deep neural network is used to achieve quantification of the CEST effect directly[32] from the undersampled saturated images. The usability of the new method is tested through numerical simulation and experiments on a creatine phantom, hen egg, and in vivo tumor rat brain.

2 | METHODS

The flow chart of CEST-PROPELLER sampling and network reconstruction is shown in Figure 1. The process of network reconstruction has three steps: (a) undersample the k-space of synthesized data with CEST-PROPELLER, (b) train the network with undersampled synthesized data, and (c) reconstruct CEST contrast images with experimental data.

2.1 | CEST-PROPELLER sampling

Generally, PROPELLER MRI continuously collects several lines from the k-space center to form a "blade," and these lines correspond to several lowest frequency phase encoded lines.[30] The number of collected lines of a blade is equal to the length of echo chain, namely the number of phases collected at one time.[33-35] In this study, different from traditional

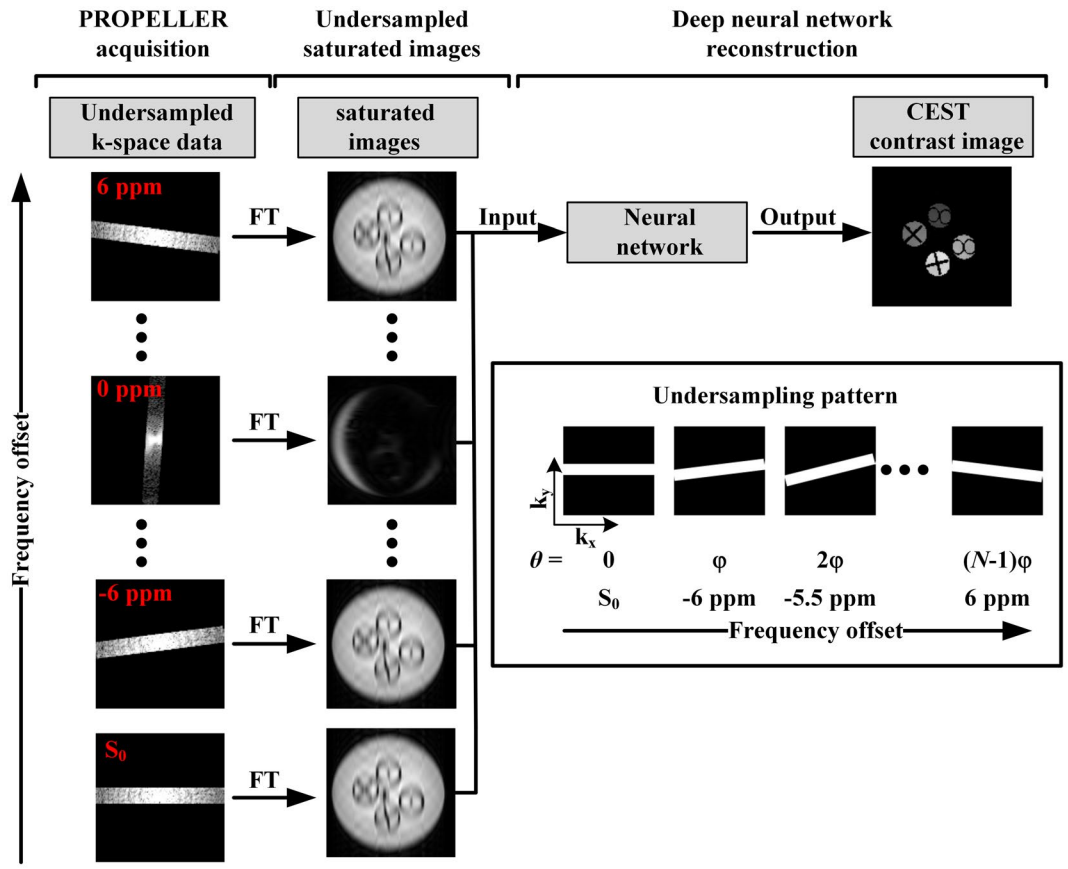

FIGURE 1 Flow chart of CEST-PROPELLER sampling and network reconstruction. The θ denotes the angle between the sampling blade and the horizontal direction, and N is the number of saturated frequency offsets

PROPELLER oversampling, only one blade of k-space is sampled for each saturated image and for different saturated images the sampling blade is successively rotated counterclockwise in the k-space by an increment of angle $\varphi = \pi/N$ (N is the number of saturated frequency offsets), so that the dataset spans a circle in the k-space. In the experiments, we collected images at 26 saturated frequency offsets, so φ was about 6.9°. Therefore, the angle of each sampling blade relative to the horizontal direction was from 0° to 173.1° with an increment of 6.9°, leading to a unique trajectory for saturated images (see Figure 1). Note that, in our work, only 16 lines were acquired for each blade per saturated image with a matrix size of 128 × 128, resulting in an acceleration factor of 8.

2.2 | Generation of synthesized data

Normally, biological tissues contain many complex compounds, such as protein molecules and amino acid molecules. The application of a saturation pulse may cause many effects in addition to the CEST effect, such as magnetization transfer (MT) effect, direct saturation (DS) effect, and nuclear Overhauser enhancement (NOE) effect.[36-40] When the power of saturation pulse is low, the process of chemical exchange between the CEST pool and the water pool is best described by the weak-saturation-pulse (WSP) approximation; whereas when the power of saturation pulse is high, the processes of interaction of direct saturation and CEST pool saturation are best predicted by the strong-saturation-pulse (SSP) approximation.[23] Our experiments satisfied the WSP approximation. Under this condition, each of the effects mentioned above in Z-spectrum can be modeled by the Lorentzian line shape model.[4,23,41] Therefore, the CEST spectrum (Z-spectrum) can be approximately decomposed into some Lorentzian curves[42,43]:

$$Z(\omega) = c - \sum_{k=1}^{P} L_k \tag{1}$$

where c is a constant, P indicates the number of exchanging proton components in the Z-spectrum, and L_k is a Lorentzian function defined by

$$L_k = \frac{A_k \cdot \Gamma_k^2/4}{\Gamma_k^2/4 + (\omega - \delta - \omega_k)^2} \tag{2}$$

where A_k is the amplitude, Γ_k is the full-width at half-maximum, ω is the frequency offset of saturation pulse, δ is the frequency shift caused by magnetic field inhomogeneity, and ω_k is the frequency offset of the proton pool k relative to the water proton pool.

According to Equation (1), we can synthesize a variety of Z-spectra. The Z-spectrum is modeled by multiple peaks at different frequency offsets. Based on previous work[44-47] and our experimental data, ω_k is fixed at 0, 2, 3.5, -2, and -4 ppm for the DS, amine, amide, MT, and NOE peaks, respectively. The amplitude (A_k) corresponding to different effect is proportional to the concentration of protons that produce the effect. There is a large amount of water and relatively small amounts of protein, polypeptide, and lipid in in vivo cases. Therefore, in the CEST experiments, the DS effect is strong, while the CEST, NOE, and MT effects are relatively weak. So, we set A_k to comply to a uniform distribution in the range of [0.6, 1], [0, 0.5], [0, 0.5], [0, 0.5], and [0, 0.5] for DS, amine, amide, MT, and NOE peaks, respectively. Usually, the NOE and MT peaks are wide, while the DS and CEST peaks are relatively narrow; hence, we set Γ_k to comply to a uniform distribution in the range of [0.5 ppm, 2 ppm], [0.3 ppm, 2 ppm], [0.3 ppm, 2 ppm], [5 ppm, 20 ppm], and [1 ppm, 10 ppm] for DS, amine, amide, MT, and NOE peaks, respectively. The distribution ranges of these parameters are large enough to cover the experimental situations.

Based on the principle of Z-spectrum generation, we can synthesize samples for neural network training. We synthesized training data with a CEST spectrum model (Equation 1) that was the summation of Lorentzian curves. The synthesized Z-spectrum includes five peaks, namely DS, amine, amide, MT, and NOE peaks (see the Results section for some representative synthesized Z-spectra). Therefore, 16 parameter maps in total (5 amplitudes A_k, 5 widths Γ_k, 5 peak positions ω_k (k = 1-5) and the frequency shift caused by magnetic field inhomogeneity δ) were needed to generate a saturated image. The δ parameter map was synthesized by a second-order surface to simulate the distribution of inhomogeneous magnetic field.

In order to add weak textures to the parameter maps, we used images containing rich textures to modulate the parameter maps A_k by element-wise multiplication. Then we took a series of values for saturation frequency offset ω and the 16 parameter maps into Equation 1 to achieve synthesized saturated images with textures. Each parameter map was composed of many random patterns with geometric textures. Therefore, the synthesized saturated images contained structural information.

Our previous work has shown that the synthesized training dataset can provide diverse structural information through random structural production, so that the structural information in the training dataset can cover various structural information of in vivo experiments as much as possible in the relatively small receptive field of ResNet (only 17 × 17 in this work).[48] The flow chart of synthesized sample generation under a series of saturation frequency offset is shown in Supporting Information Figure S1, which is available online.

In this work, the saturation frequency offset ω was set from -6 ppm to 6 ppm with an increment of 0.5 ppm for 25 saturated images, together with a saturation frequency

offset of 100 ppm for unsaturated image for intensity normalization. Thus, a training sample contained 25 saturated images and 1 unsaturated image. In total, 3000 training samples with a size of 128 × 128 each were generated by MATLAB 8.3.0.532 (R2014a) software (Mathworks, Natick, MA, USA). Each sample corresponds to two ground-truth CEST contrast images at 2 ppm and 3.5 ppm. Therefore, the synthesized training dataset can be applied for different target neural network reconstruction provided that CEST effect appears at 2 ppm or 3.5 ppm. The source code used for sample synthesis is available on reasonable request.

2.3 | Network training

The classical U-Net[49] was used to reconstruct CEST contrast images. The k-space data of synthesized saturated images were retrospectively undersampled by our PROPELLER scheme and processed by Fourier transform to obtain images X as the input of network. The label Y was the CEST contrast image of the interested exchanged protons. The pixel-wise mean squared error (MSE) was calculated as

$$L_{MSE} = \frac{1}{M}\sum_{i=1}^{M} \left\| f(X_i, \mathbf{W}, \mathbf{b}) - Y_i \right\|_2^2 \tag{3}$$

where M is the batch size, $f(\cdot)$ is the deep neural network, $\mathbf{W}$ and $\mathbf{b}$ are network parameters needed to be trained. MSE is widely used as the loss function for image super-resolution reconstruction.[50] However, the use of MSE as loss function may produce blurry images, so we used an image gradient difference loss (GDL) function[51] as a compensation to keep the regions with strong gradients and better model the nonlinear mapping from source to target. It is defined as

$$L_{\mathrm{GDL}}(Y, \hat{Y}) = \left| \left|\nabla Y_x\right| - \left|\nabla \hat{Y}_x\right| \right|^2 + \left| \left|\nabla Y_y\right| - \left|\nabla \hat{Y}_y\right| \right|^2 \tag{4}$$

where Y and $\hat{Y}$ denote the ground-truth target image and the estimated target image respectively, and the subscripts x and y denote the dimension direction of images. The use of this loss function can minimize the difference of the gradient magnitudes between the ground-truth target image and the estimated target image. The final loss function is then expressed as

$$\mathrm{Loss} = L_{\mathrm{MSE}} + \lambda L_{\mathrm{GDL}} \tag{5}$$

where λ is a weight ($\lambda = 0.8$ in this work). To train the deep neural network, we used 3000 synthesized samples mentioned above. These samples were randomly split into training and validation sets: 80% for training and 20% for validation. All these samples were randomly cropped into 64 × 64, and the batch size was 16. Considering the presence of noise in practical experiments, we added Gaussian noise with a mean value of 0 and an SD of 1% to the samples before training. The initial learning rate was set to 0.0001 and then decreased by a factor of 5 after 50 000 times of iteration. It took nearly 12 hours for training to complete 500 000 iterations on a machine with one GTX1080Ti GPU.

2.4 | Sample preparation

Amine protons in creatine lead to an obvious CEST effect with a frequency offset of 2 ppm from water. Therefore, a phantom containing four tubes of creatine in normal saline with different concentrations was used. Different shapes of plastic sheets were immersed in creatine solution to increase image details to better confirm the feasibility of CEST-PROPELLER MRI. The four tubes were immersed in a large tube filled with normal saline, which facilitated shimming to get a uniform magnetic field. The concentrations of creatine solution were 20, 40, 60 and 80 mM, respectively (pH = 7.2). Fresh hen egg contains many complex compounds, such as fat, cholesterol, and proteins with amino acids. It was used as simple biological tissues to demonstrate the amide proton transfer (APT) effect. A Sprague-Dawley rat was anesthetized by a continuous flow of 2%-3% isoflurane. Using Bregma as a reference, a 1 mm burr hole was made 2 mm anterior and 2.5 mm lateral. 100 000 rat 9L glioma cells in 10 μL of sterile phosphate buffer saline (PBS) were injected at a depth of 3.5 mm from the skull. MRI experiment of the in vivo tumor rat was performed 11 days after the tumor cells were implanted. All of the operations throughout the experimental procedures were handled in accordance with protocols approved by the ethical committee of the Florida State University (FSU) Animal Care and Use Committee.[52]

2.5 | Data acquisition

Experiments of creatine phantom and egg were performed on a 7.0T Varian MRI system with a horizontal Magnex magnet, equipped with 100 mm bore imaging gradients (40 G/cm). Experiment of tumor rat was performed on a 21.1T Bruker system with a horizontal Magnex magnet, equipped with 105 mm bore imaging gradients (60 G/cm). In the rat brain experiment, a custom-built quadrature double-saddle surface coil was used to transmit and receive the signal. This coil was equipped with a bite-bar that together with hook-and-loop straps to suspend and secure the animal in the magnet. The bite-bar also supplied the rat with continuous flow of anesthesia. Prior to in vivo imaging, the animal

was anesthetized with 5% isoflurane; and then lowered to 2% and adjusted to maintain a respiratory rate between 30 and 40 breaths/min as monitored with a pneumatic pillow situated under the animal (SA Instruments Inc., Stony Brook, NY). CEST-FSE experiments were performed for references and CEST-PROPELLER undersampling.

Experiments were performed at 25°C. Experimental parameters for acquisition were set as follows: acquisition matrix = 128 × 128, slice thickness of creatine phantom and egg = 1 mm, slice thickness of rat = 2 mm. According to previous reports,[53,54] the RF saturation power was set to 1.8 μT/1.2 μT/1.5 μT and the saturation time was set to 2 s/3 s/4 s for creatine/egg/rat respectively. Repetition time = 6 s was selected to provide sufficient time for the longitudinal magnetization of water to fully recover for the successive acquisition. The saturation pulse frequency was swept from −6 to 6 ppm with an increment of 0.5 ppm, and an image with saturation pulse frequency applied at 100 ppm was also acquired as unsaturated image for signal normalization. The echo train length (ETL) was 8 and the single-slice scan time for creatine/egg/rat was 55.4 min/62.4 min/69.4 min. The water saturation shift-referencing (WASSR) method[45] (a single 200 ms saturation pulse with 0.5 μT amplitude) was used to correct the water frequency shifts for these experiments. The k-space data of saturated images from CEST-FSE were retrospectively undersampled using CEST-PROPELLER scheme with an undersampling rate of 8. Theoretically, this means the scan time of our method for creatine/egg/rat can be reduced to 6.9 min/7.8 min/8.7 min. For comparison, the full Lorentzian fitting with multiple pools[55] was applied to the fully sampled images of CEST-FSE to obtain CEST contrast images as references, and the threshold value of the Lorentzian fitting was set as half of the minimum normalized signal intensity of the model area to rule out the background noises. The boundary conditions for the full Lorentzian fitting were the same as those used in synthesizing training samples.

3 | RESULTS

3.1 | Numerical simulations

A synthesized saturated image and the corresponding CEST contrast image obtained using different methods are shown in Figure 2. As can be seen from Figure 2E, the difference

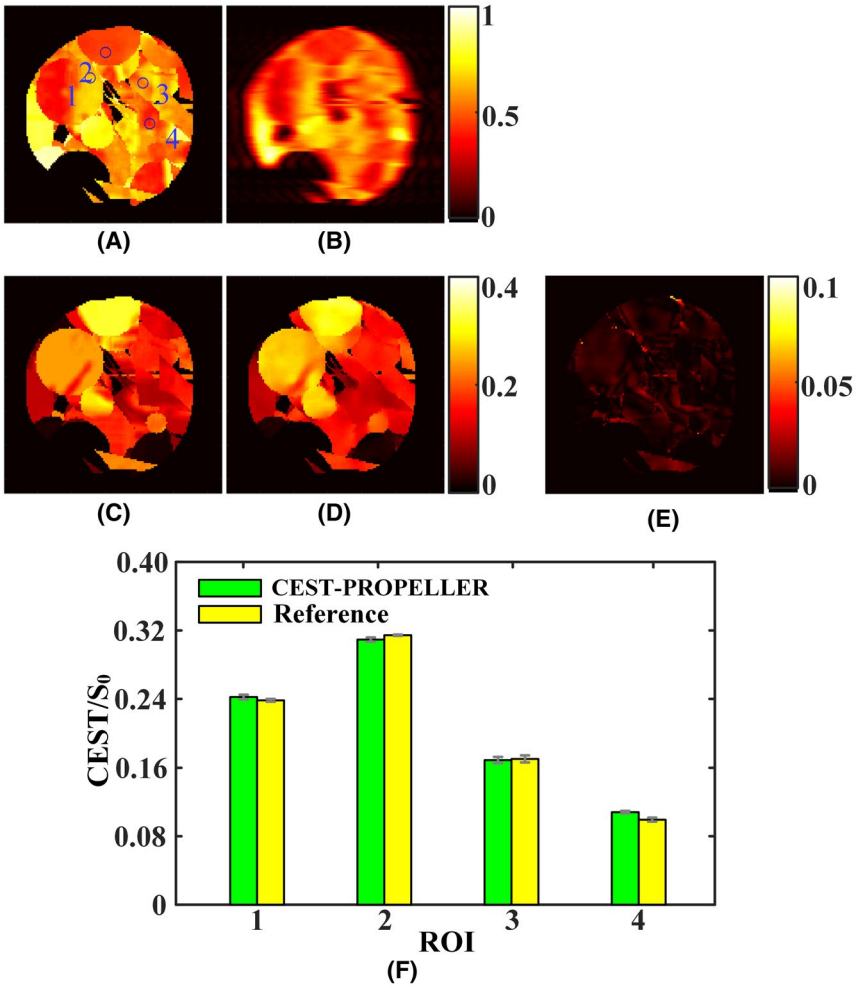

FIGURE 2 The results of numerical simulation. Field of view = 60 mm × 60 mm. Each image matrix was 128 × 128. A, Synthesized saturated image at 2 ppm. B, Saturated image undersampled from (A) using CEST-PROPELLER. C, CEST contrast image (at 2 ppm) reconstructed from synthesized saturated images as the reference. D, CEST contrast image (at 2 ppm) reconstructed from CEST-PROPELLER images. E, Difference map between (C) and (D). F, Mean CEST values and standard deviations (shown as vertical bars) for the four regions of interest (ROIs) marked in (A) from the reference and the result of CEST-PROPELLER

between Figure 2C,D is small. The Pearson's correlation coefficient between Figure 2C,D is 0.9901. These indicate that reliable result can be obtained using CEST-PROPELLER with an undersampling rate of 8. The texture features of the CEST-PROPELLER result are slightly lost, which may be caused by the high undersampling rate. Four ROIs were selected to calculate the mean CEST values and the SDs. The numerical differences between the CEST-PROPELLER result and the reference can be found in Figure 2F. The relative CEST signal intensities of CEST-PROPELLER are almost equal to the reference ones in all four ROIs, which reveals the accuracy of reconstructed CEST values.

3.2 | Phantom validation

Figure 3 shows the comparison of the synthesized and actually measured Z-spectra of creatine phantom. The frequency offset of the amine protons of creatine is about 2 ppm on the Z-spectrum. A significant CEST effect appears at 2 ppm on the Z-spectrum. The Z-spectrum of creatine can be fitted out easily. We can see that the synthesized and the measured Z-spectra are almost the same. Figure 4 shows an originally acquired saturated image and CEST contrast image under a homogenous field using the CEST-FSE and the corresponding results from CEST-PROPELLER undersampling. It can be seen from Figure 4A that the four tubes of creatine solution contain some details. Due to high undersampling rate, the information of the tube edges and details of the saturated image obtained from CEST-PROPELLER is severely lost (Figure 4B). However, the CEST contrast image obtained with CEST-PROPELLER agrees well with the CEST contrast image obtained with CEST-FSE (Figure 4E). The structural and texture features are well reconstructed. The Pearson's correlation coefficient between Figure 4C,D is 0.9924. The mean CEST values and the SDs for the four ROIs marked in Figure 4A are calculated and the results are given in Figure 4F, indicating the great consistency between these two CEST results.

3.3 | Hen egg study

Fresh eggs contain rich compounds such as polypeptides, lipids, and other macromolecules. Therefore, the Z-spectrum of egg contains MT, CEST, NOE, and DS effects. Egg white is a kind of gelatinous, translucent liquid mixture that contains about 11% protein, so it can be used to prove the APT effect. Figure 5 shows the comparison of the synthesized and the actually measured Z-spectra of egg white. Although the Z-spectrum of egg white is relatively complex, we can still synthesize a very similar Z-spectrum. The APT imaging results of fresh hen egg are shown in Figure 6. From Figure 6C,D, we can see that both of the APT images obtained using CEST-FSE and CEST-PROPELLER remain good shapes. The results from these two methods agree well with each other (Figure 6E). The Pearson's correlation coefficient between Figure 6C,D is 0.9791. The mean APT values and the SDs for the five ROIs marked in Figure 6A are calculated, and the results are given in Figure 6F. Comparing the reconstructed results of creatine phantom and hen egg from CEST-PROPELLER, we can see that the result of creatine phantom is better than that of egg. Perhaps it is because the egg contains more substances, and these substances may cause other effects when the saturated pulse is applied, which makes the situation more complicated and the reconstruction more difficult.

3.4 | In vivo tumor rat imaging

The Z-spectra generated by our simulation and obtained from the in vivo tumor rat experiment are displayed in Figure 7. We took the regions indicated by blue dots in the rat brain for

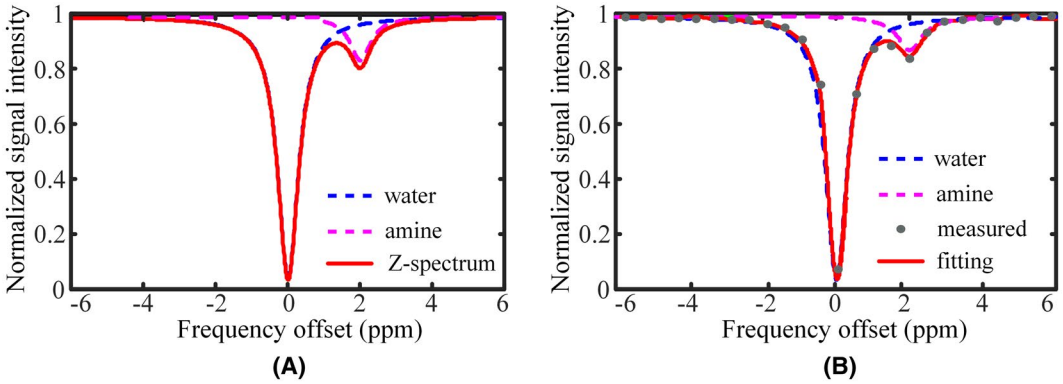

FIGURE 3 Comparison of the synthesized and actual measured Z-spectra of creatine phantom. A, A synthesized Z-spectrum. The water pool and amine pool are respectively indicated by dashed lines of different colors. The two pools are superimposed to get the final Z-spectrum, which is indicated by a solid red line. B, A Z-spectrum acquired from the creatine phantom

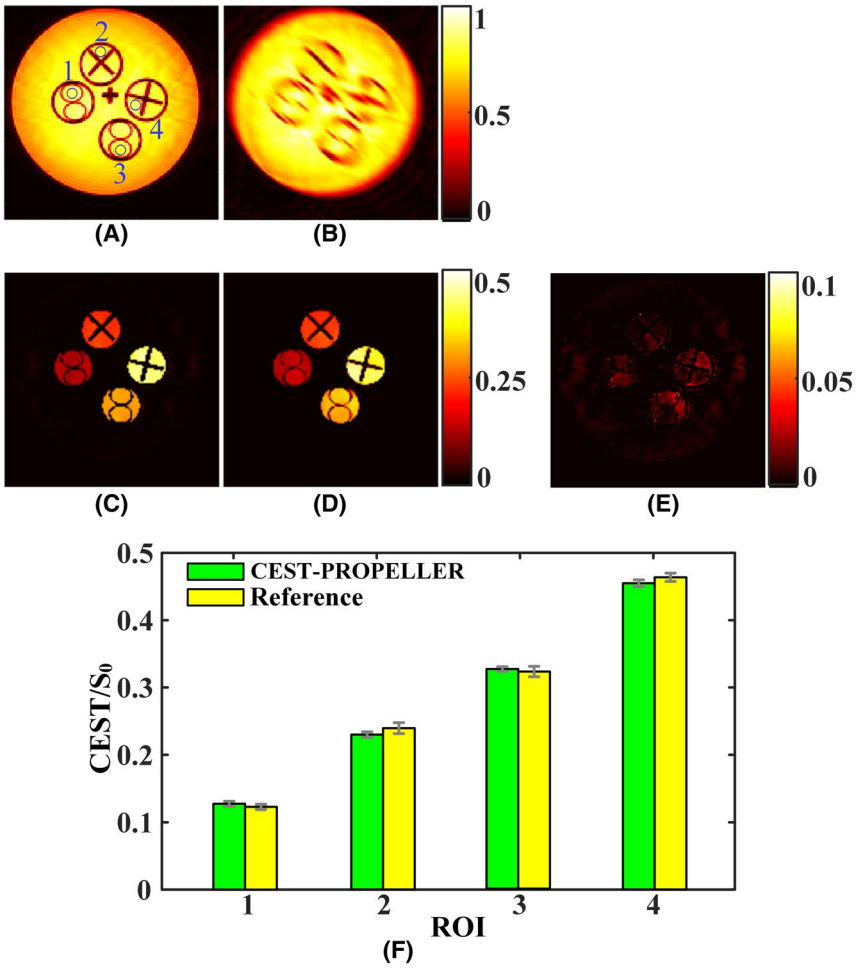

FIGURE 4 The results of creatine phantom experiment. Field of view = 60 mm × 60 mm. A, Saturated image at 2 ppm obtained using CEST-FSE. B, Saturated image undersampled from (A) using CEST-PROPELLER. C, CEST contrast image (at 2 ppm) reconstructed from CEST-FSE images as a reference. D, CEST contrast image (at 2 ppm) reconstructed from CEST-PROPELLER images. E, Difference map between (C) and (D). F, Mean CEST values and standard deviations (shown as vertical bars) for the four regions of interest (ROIs) marked in (A) from CEST-FSE and CEST-PROPELLER methods. The creatine concentrations for ROI 1 to ROI 4 are 20, 40, 60 and 80 mM, respectively

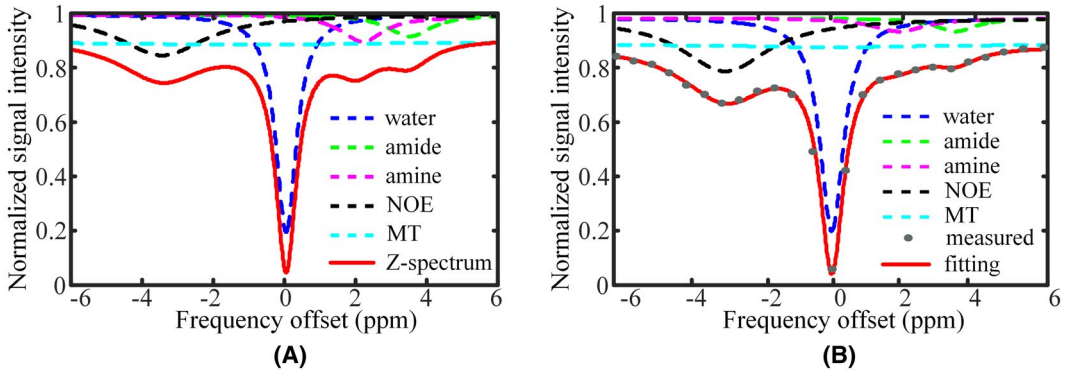

FIGURE 5 Comparison of the synthesized and actual measured Z-spectra of a fresh egg. A, A synthesized Z-spectrum. The water pool, amine pool, amide pool, NOE pool, and MT pool are respectively indicated by dashed lines of different colors. These pools are superimposed to get the final Z-spectrum, which is indicated by a solid red line. B, A Z-spectrum acquired from the egg white

Z-spectra comparison. Regions 1 and 2 are in the tumor area and regions 3 and 4 are outside the tumor area (Figure 7A). The Z-spectra of regions 1-4 are displayed in Figures 7D-G, respectively. Comparing Figures 7B,C with Figures 7D-G, we can see that the synthesized Z-spectra are more similar to the acquired Z-spectra in the tumor area than the acquired Z-spectra outside the tumor area. The imaging results of a tumor rat brain are displayed in Figure 8. From Figure 8C,D, we can see that both of the APT images obtained using CEST-FSE and CEST-PROPELLER show high signal intensity in the tumor area (the approximate region invaded by the glioma is indicated by the red contour in Figure 8A). Compared with Figure 8A, both Figure 8C,D well show the tumor area. The difference between Figure 8C,D is relatively small in tumor area (Figure 8E). This indicates that our method can detect the tumor area in the rat brain.

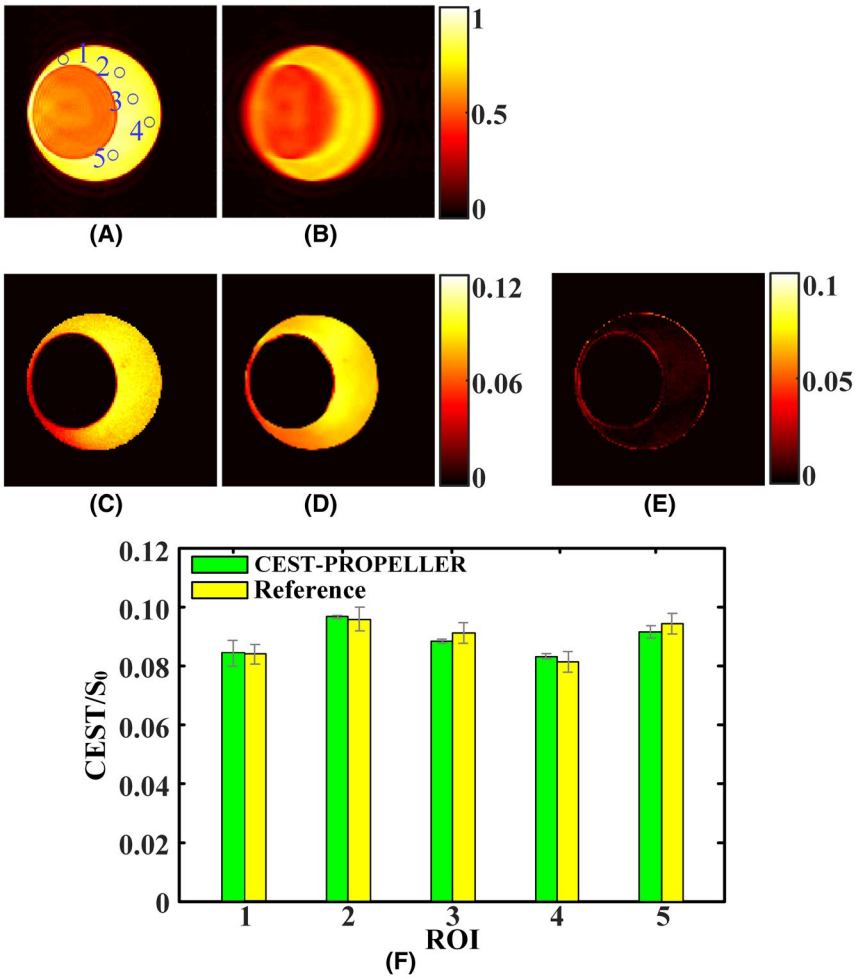

FIGURE 6 The results of fresh hen egg experiment. Field of view = 60 mm × 60 mm. A, Saturated image at 3.5 ppm obtained using CEST-FSE. B, Saturated image undersampled from (A) using CEST-PROPELLER. C, APT image (at 3.5 ppm) reconstructed from CEST-FSE images as a reference. D, APT image (at 3.5 ppm) reconstructed from CEST-PROPELLER images. E, Difference map between (C) and (D). F, Mean APT values and SDs (shown as vertical bars) for the five regions of interest (ROI) marked in (A) from CEST-FSE and CEST-PROPELLER methods

4 | DISCUSSION

CEST-PROPELLER can greatly reduce the acquisition time for CEST imaging. A CEST contrast image can be obtained directly using the trained reconstruction network within milliseconds, whereas it takes a few minutes to obtain a CEST contrast image by using traditional Z-spectra fitting method.

MRI image reconstruction via neural network requires a large volume of experimental data for network training. Due to the lack of experimental data, we used the mathematical model[42,43] to synthesize training data. Although it is an approximation to assume that the CEST spectrum is an addition of Lorentzian curves, it is a simple approach with acceptable error. A large parameter space is adapted in the generation of synthesized data to cover the whole parameter space of experimental data as much as possible and make the synthesized data consistent with the experimental data. Our group has successfully realized the T_2 mapping with synthesized data.[48,56] To the best of our knowledge, this is the first study combining the PROPELLER approach with deep neural network to accelerate CEST imaging.

Simulation and experimental results show that an acceleration factor of 8 for CEST-PROPELLER can be achieved almost without compromising the quality of reconstructed CEST contrast image. Although the saturated image of each frequency offset is undersampled, there is redundancy between the saturated images. Deep learning can mine the redundancy between images to ensure the quality of reconstruction. In addition, because the influence of magnetic field inhomogeneity has been taken into account when training data are generated, our method can yield accurate CEST contrast images without WASSR method. Note that, in our experiments, FSE-CEST is used to acquire fully sampled saturated images, and FSE has good resistance to inhomogeneous magnetic field. Therefore, the acquired signals are mainly affected by T_2 decay, which may lead to the blurring of images, and the signal decay caused by magnetic field inhomogeneity can be neglected.

For the CEST-PROPELLER method, there are two main factors that affect the reconstructed results. The first factor is the differences between synthesized data and experimental data. Apparently, the training dataset plays a decisive role for the network in learning the nonlinear mapping relationship from CEST-PROPELLER images to the corresponding CEST contrast image. Since there are inherent errors in the mathematical modeling of practical problems, the synthesized data

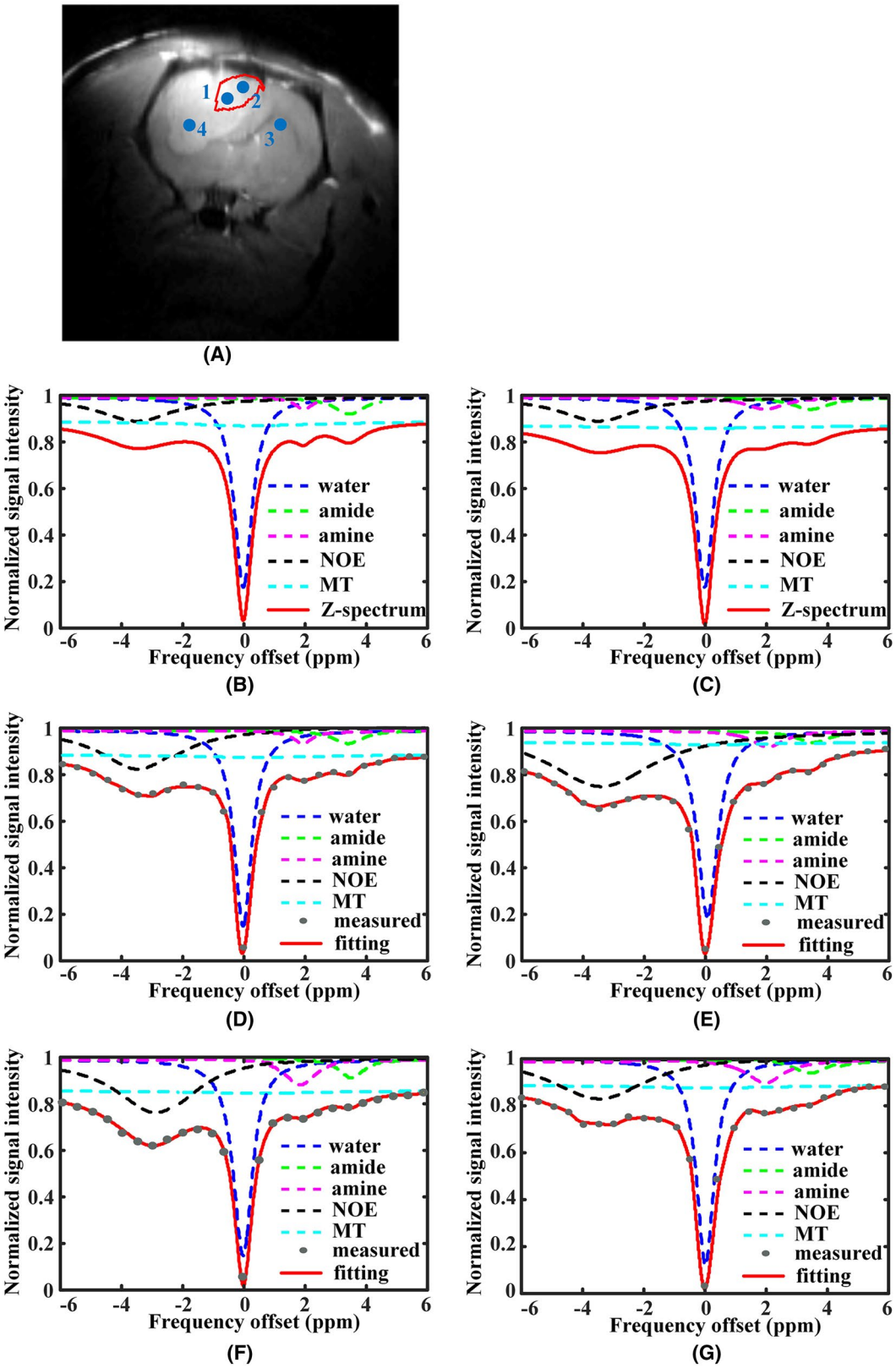

FIGURE 7 Comparison of Z-spectra. A, Saturated image at 3.5 ppm obtained using FSE-CEST. The approximate region invaded by the glioma is indicated by the red contour. Four regions labeled 1-4 are selected for comparison. B and C, Examples of the synthesized Z-spectra. D, The acquired Z-spectrum of region 1. E, The acquired Z-spectrum of region 2. F, The acquired Z-spectrum of region 3. G, The acquired Z-spectrum of region 4. Each Z-spectrum is decomposed into several Lorentzian curves and the free water pool, amine proton pool, amide proton pool, NOE pool, and MT pool are respectively indicated by dashed lines of different colors

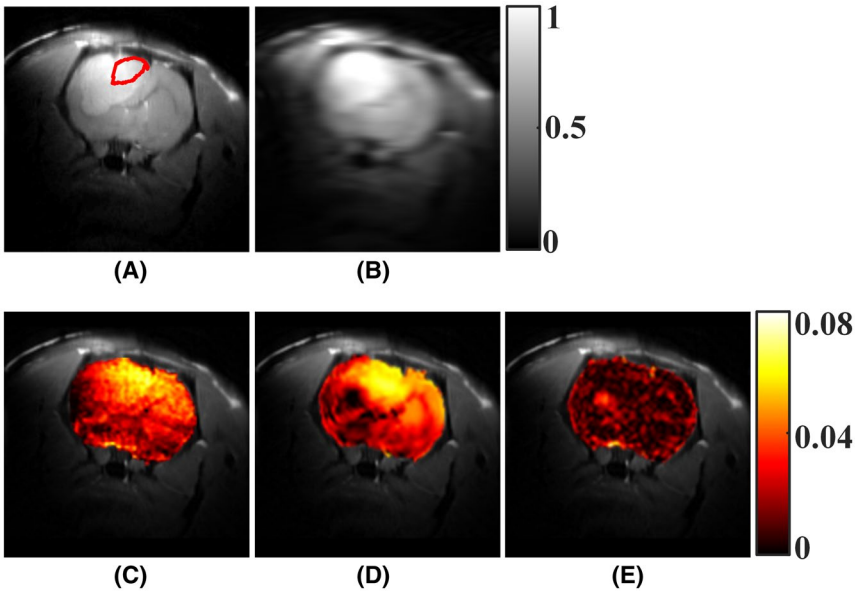

FIGURE 8 The results of a tumor rat brain experiment. Field of view = 25 mm × 25 mm. A, Saturated image at 3.5 ppm obtained using CEST-FSE. B, Saturated image undersampled from (A) using CEST-PROPELLER. C, APT image (at 3.5 ppm) reconstructed from CEST-FSE images as a reference. D, APT image (at 3.5 ppm) reconstructed from CEST-PROPELLER images. E, Difference map between (C) and (D)

could not be exactly the same as the experimental data. The differences will cause a negative impact on the reconstructed results. This may be the reason for the observable differences between Figure 8C,D, especially in normal area.

As we have described in the Methods section, the CEST spectrum model (Equations 1 and 2) was used for training data generation. This model simplifies the CEST spectrum to superposition of Lorentzian curves. It cannot simulate the Z-spectra of super-Lorentzian line shape, and the simulated Z-spectra only contain a few of known CEST pools, MT pool, NOE pool, and DS pool.[32] Therefore, the simulated Z-spectra may not completely cover various Z-spectra acquired in in vivo experiments. Note that for CEST imaging, it is more important to correctly detect tumor area, and the present CEST spectrum model works well at this aspect. The reason that the CEST spectrum model works better in the tumor area than in the normal area may be because the known CEST effects are stronger in the tumor area, leading to relatively smaller influence of imperfect CEST spectrum model for the tumor area. Further improvement, especially for the normal area, may be achieved in the future with the knowledge of more CEST pools and the consideration of super-Lorentzian line shape.

The second factor is the undersampling rate. Obviously, the lower the undersampling rate, the longer the acquisition time required. However, if the undersampling rate is too high, the original information will be seriously lost, which will make the network learning task complicated and the accuracy of reconstructed result decreased. In our work, we use the CEST-PROPELLER sampling method to extract 16 lines from the k-space of 128 × 128 size, so the undersampling rate is 8. The resulting CEST contrast images are in good agreement with the references.

To explore the effect of the undersampling rate on reconstructed results, we constructed four sets of undersampled data by extracting 10, 16, 21 and 32 lines from the full k-space, which corresponded to undersampling rates of 12.8, 8, 6.1 and 4, respectively. The reconstructed results are given in Figure 9. The higher the undersampling rate, the fuzzier the saturated images. When the undersampling rate is 12.8, the APT image shows severe signal loss (yellow arrows in Figure 9G). As the undersampling rate decreases, this situation is alleviated and the difference between the result and the reference becomes smaller (Figures 9K-N). When the undersampling rates are 12.8, 8, 6.1 and 4, the Pearson's correlation coefficients between Figure 9B,G-J are 0.9694, 0.9791, 0.9798 and 0.9804, respectively. The mean APT values and the SDs for the five ROIs marked in Figure 9A are calculated and the results are given in Figure 10. We can see that the results of CEST-PROPELLER are more and more consistent with the results of CEST-FSE with the decrease of undersampling rate. However, the accuracy improvement of the reconstructed result is at the expense of scan time.

Recently, a deep feed-forward neural network, including a probabilistic output layer allowing for uncertainty quantification, was set up to take uncorrected CEST-spectra as input and predict 3T Lorentzian parameters of a four-pool model (water, semisolid MT, amide CEST, and NOE CEST), including the B_0 inhomogeneity.[32] Although the method is similar to our method, there are some differences between them. In the published work, in vivo Z-spectra were acquired at 3T, and then the fully sampled Z-spectra were used to train the deep neural network to directly map Lorentzian parameters. In this work, we introduce the PROPELLER sampling scheme into CEST imaging to shorten the acquisition time. Undersampled synthesized saturated images are used to train the U-Net, and the CEST contrast images are obtained directly using the trained reconstruction network.

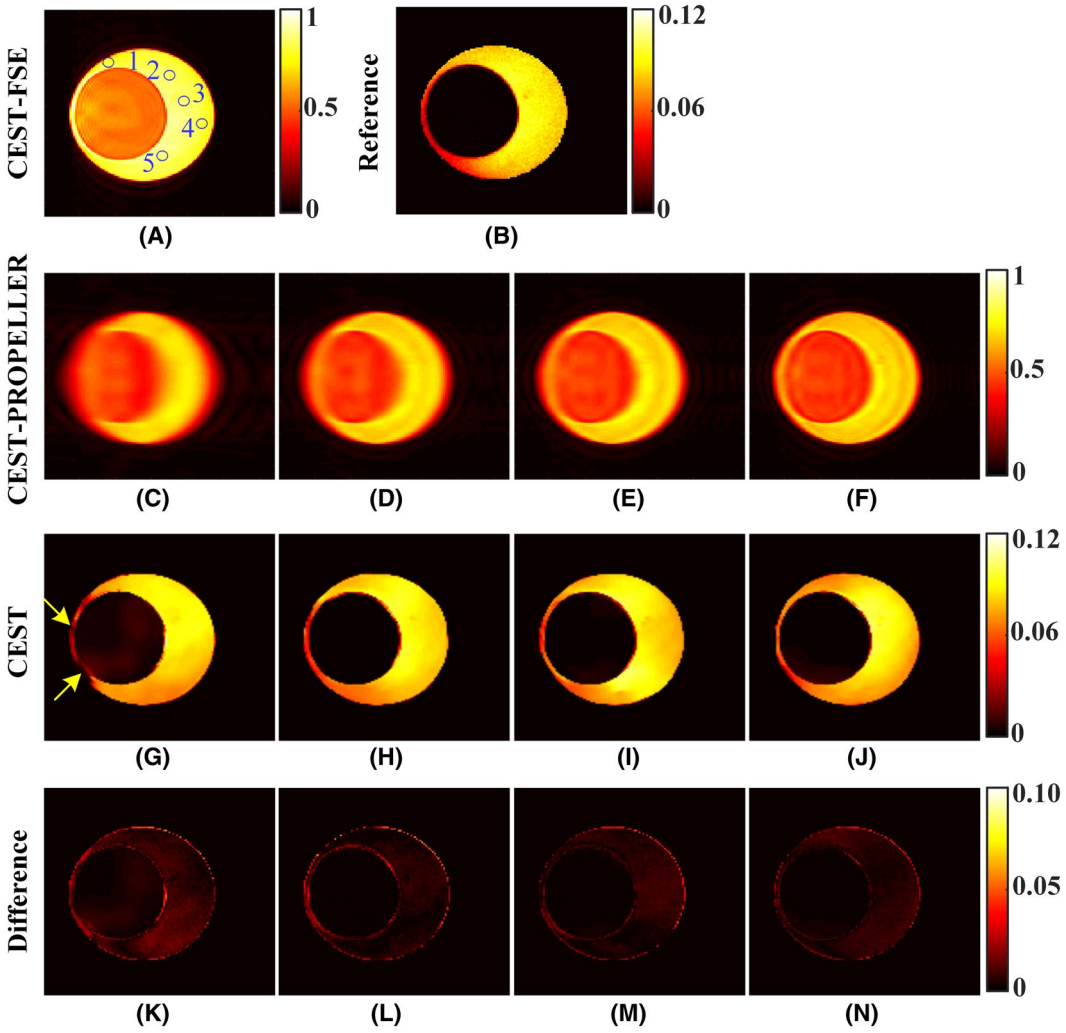

FIGURE 9 Images of fresh hen egg obtained with different methods. Field of view = 60 mm × 60 mm. A, Saturated image at 3.5 ppm obtained using CEST-FSE. B, APT image (at 3.5 ppm) reconstructed from CEST-FSE images as a reference. C-F, Saturated images obtained from (B) using CEST-PROPELLER with undersampling rates of 12.8, 8, 6.1, and 4, respectively. G-J, APT images (at 3.5 ppm) reconstructed from CEST-PROPELLER images with undersampling rates of 12.8, 8, 6.1, and 4, respectively. K-N, Difference maps between (G-J) and the reference (B). The five regions of interest in (A) indicated with blue circles were used to calculate the APT values

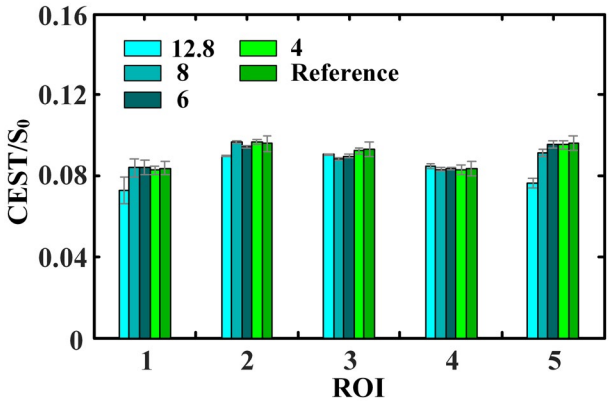

FIGURE 10 Comparison of the mean CEST values and SDs (shown as vertical bars) for the five regions of interest (ROIs) marked in (Figure 9A) between CEST-PROPELLER with 12.8, 8, 6.1, and 4 undersampling rates and CEST-FSE methods

As mentioned in the above publication, the MSE between the inputs and outputs of the trained network cannot be reduced for training samples with similar inputs but different targets. We found that the combination of MSE loss function with gradient difference loss (GDL) function[51] give good predictions. So, we used this combination (Equation 5) as the final loss function of the neural network. For comparison, a non-GDL U-Net was also trained to predict CEST contrast images. This network was trained by using the MSE as loss function but excluding GDL function. The reconstructed results of three simulated data from the networks with different loss functions show better performance of the network with GDL function (see Supporting Information Figure S2). The Pearson's correlation coefficients between reference images and images reconstructed with GDL are 0.9933, 0.9863, and 0.9936, respectively, and the Pearson's correlation coefficients

between reference images and images reconstructed without GDL are 0.9887, 0.9782, and 0.9829, respectively.

In this proof of concept study, fully sampled CEST-FSE data were used for CEST-PROPELLER acquisition to verify the feasibility and advantage of the CEST-PTOPELLER sampling strategy. Similar method has been taken to verify the feasibility of CS-SENSE approach for accelerating APT imaging.[31] The PROPELLER undersampling strategy is relatively easy to implement and can considerably accelerate CEST imaging. When we generated the synthesized PROPELLER data for training and testing the neural network, we have considered the influence of magnetic field inhomogeneity and noise so as to reduce the difference between our synthesized data and the real data acquired from PROPRLLER pulse sequence. However, there are still some factors existing in practical experiments that we did not consider, such as the eddy current effect and turbo spin echo (TSE) order. The difference between the synthesis and actual acquisition may decrease the performance of our method, but it would not alter our conclusion. Direct application of CEST-PROPELLER pulse sequence, including consideration of more influence factors in training data synthesis, deserves further study.

The CEST-PROPELLER acquisition for scan time saving is similar to the snapshot-CEST approaches like snapshot-CEST approach[57] and snapshot 3D-EPI CEST approach,[25] namely one saturation block per offset and only one readout for one offset image. The snapshot 3D-EPI CEST approach acquires the whole-brain imaging volume after a single saturation block within a very short scan time. We can translate present CEST-PROPELLER to 3D CEST imaging by replacing its readout module with the 3D EPI readout module used in the snapshot 3D-EPI CEST approach. This would unleash the power of CEST-PROPELLER. However, due to the vulnerability of EPI to inhomogeneous fields, its implementation should be in relatively homogeneous fields to yield good results.

5 | CONCLUSIONS

CEST provides a unique MRI contrast approach that breaks the inherent sensitivity limitation of traditional MRI methods and has great potential in disease diagnosis. In this study, we introduce a fast CEST MRI method based on PROPELLER undersampling and deep neural network reconstruction. This method offers a significant scan time reduction. The feasibility of CEST-PROPELLER MRI is demonstrated through creatine phantom, fresh hen egg, and in vivo tumor rat brain experiments. The experimental results show that CEST-PROPELLER can provide good CEST contrast images. With further improvement, this technique may find applications in clinical diagnosis.

ACKNOWLEDGMENTS

The authors thank Prof. Lucio Frydman (Weitzman Institute of Science), Ms Shannon Helsper, and Dr. Ali Darkazalli (Florida State University) for technical and surgical assistance, and Professor Cathy Levenson (Florida State University) for providing the 9L glioma cells and helpful insights into the glioma animal model.

ORCID

Shuhui Cai https://orcid.org/0000-0003-2767-9490

REFERENCES

1. Jones KM, Pollard AC, Pagel MD. Clinical applications of chemical exchange saturation transfer (CEST) MRI. *J Magn Reson Imaging*. 2018;47:11-27.
2. Msayib Y, Harston G, Tee YK, et al. Quantitative CEST imaging of amide proton transfer in acute ischaemic stroke. *Neuroimage Clin*. 2019;23:101833.
3. van Zijl PCM, Yadav NN. Chemical exchange saturation transfer (CEST): what is in a name and what isn't? *Magn Reson Med*. 2011;65:927-948.
4. Zaiss M, Bachert P. Chemical exchange saturation transfer (CEST) and MR Z-spectroscopy in vivo: a review of theoretical approaches and methods. *Phys Med Biol*. 2013;58:R221-R269.
5. Lindeman LR, Randtke EA, High RA, Jones KM, Howison CM, Pagel MD. A comparison of exogenous and endogenous CEST MRI methods for evaluating in vivo pH. *Magn Reson Med*. 2018;79:2766-2772.
6. Zhang X-Y, Wang F, Li H, et al. Accuracy in the quantification of chemical exchange saturation transfer (CEST) and relayed nuclear Overhauser enhancement (rNOE) saturation transfer effects. *NMR Biomed*. 2017;30:e3716.
7. Zhou JY, van Zijl PCM. Chemical exchange saturation transfer imaging and spectroscopy. *Prog Nucl Mag Res Sp*. 2006;48:109-136.
8. Goerke S, Zaiss M, Bachert P. Characterization of creatine guanidinium proton exchange by water-exchange (WEX) spectroscopy for absolute-pH CEST imaging in vitro. *NMR Biomed*. 2014;27:507-518.
9. Lee JS, Xia D, Jerschow A, Regatte RR. In vitro study of endogenous CEST agents at 3T and 7T. *Contrast Media Mol Imaging*. 2016;11:4-14.
10. Longo DL, Bartoli A, Consolino L, et al. In vivo imaging of tumor metabolism and acidosis by combining PET and MRI-CEST pH imaging. *Cancer Res*. 2016;76:6463-6470.
11. Longo DL, Sun PZ, Consolino L, Michelotti FC, Uggeri F, Aime S. A general MRI-CEST ratiometric approach for pH imaging: demonstration of in vivo pH mapping with lobitridol. *J Am Chem Soc*. 2014;136:14333-14336.
12. Li C, Peng S, Wang R, et al. Chemical exchange saturation transfer MR imaging of Parkinson's disease at 3 Tesla. *Eur Radiol*. 2014;24:2631-2639.
13. Yuwen Zhou I, Wang E, Cheung JS, et al. Direct saturation-corrected chemical exchange saturation transfer MRI of glioma: simplified decoupling of amide proton transfer and nuclear Overhauser effect contrasts. *Magn Reson Med*. 2017;78:2307-2314.
14. Liu H, Jablonska A, Li Y, et al. Label-free CEST MRI detection of citicoline-liposome drug delivery in ischemic stroke. *Theranostics*. 2016;6:1588-1600.

15. Sun PZ, Cheung JS, Wang EF, Lo EH. Association between pH-weighted endogenous amide proton chemical exchange saturation transfer MRI and tissue lactic acidosis during acute ischemic stroke. *J Cereb Blood Flow Metab*. 2011;31:1743-1750.
16. Tietze A, Blicher J, Mikkelsen IK, et al. Assessment of ischemic penumbra in patients with hyperacute stroke using amide proton transfer (APT) chemical exchange saturation transfer (CEST) MRI. *NMR Biomed*. 2014;27:163-174.
17. Chen H, Liu D, Li Y, et al. CEST MRI monitoring of tumor response to vascular disrupting therapy using high molecular weight dextrans. *Magn Reson Med*. 2019;82:1471-1479.
18. Chan KWY, McMahon MT, Kato Y, et al. Natural D-glucose as a biodegradable MRI contrast agent for detecting cancer. *Magn Reson Med*. 2012;68:1764-1773.
19. Xu JZ, Zaiss M, Zu ZL, et al. On the origins of chemical exchange saturation transfer (CEST) contrast in tumors at 9.4 T. *NMR Biomed*. 2014;27:406-416.
20. Zhang YI, Heo H-Y, Lee D-H, et al. Chemical exchange saturation transfer (CEST) imaging with fast variably-accelerated sensitivity encoding (vSENSE). *Magn Reson Med*. 2017;77:2225-2238.
21. Zhou J, Zhu HE, Lim M, et al. Three-dimensional amide proton transfer MR imaging of gliomas: initial experience and comparison with gadolinium enhancement. *J Magn Reson Imaging*. 2013;38:1119-1128.
22. Dixon WT, Hancu I, Ratnakar SJ, Sherry AD, Lenkinski RE, Alsop DC. A multislice gradient echo pulse sequence for CEST imaging. *Magn Reson Med*. 2010;63:253-256.
23. Zaiss M, Schmitt B, Bachert P. Quantitative separation of CEST effect from magnetization transfer and spillover effects by Lorentzian-line-fit analysis of Z-spectra. *J Magn Reson*. 2011;211:149-155.
24. Zaiss M, Xu JZ, Goerke S, et al. Inverse Z-spectrum analysis for spillover-, MT-, and T_1-corrected steady-state pulsed CEST-MRI application to pH-weighted MRI of acute stroke. *NMR Biomed*. 2014;27:240-252.
25. Akbey S, Ehses P, Stirnberg R, Zaiss M, Stocker T. Whole-brain snapshot CEST imaging at 7T using 3D-EPI. *Magn Reson Med*. 2019;82:1741-1752.
26. Ellingson BM, Yao J, Raymond C, et al. pH-weighted molecular MRI in human traumatic brain injury (TBI) using amine proton chemical exchange saturation transfer echoplanar imaging (CEST EPI). *Neuroimage Clin*. 2019;22:101736.
27. Jiang WP, Zhou IY, Wen LY, Zhou X, Sun PZ. A theoretical analysis of chemical exchange saturation transfer echo planar imaging (CEST-EPI) steady state solution and the CEST sensitivity efficiency-based optimization approach. *Contrast Media Mol Imaging*. 2016;11:415-423.
28. Togao O, Keupp J, Hiwatashi A, et al. Amide proton transfer imaging of brain tumors using a self-corrected 3D fast spin-echo dixon method: comparison with separate B_0 correction. *Magn Reson Med*. 2017;77:2272-2279.
29. Zhang Y, Yong XW, Liu RB, et al. Whole-brain chemical exchange saturation transfer imaging with optimized turbo spin echo readout. *Magn Reson Med*. 2020;84:1161-1172.
30. Pipe JG. Motion correction with PROPELLER MRI: application to head motion and free-breathing cardiac imaging. *Magn Reson Med*. 1999;42:963-969.
31. Heo HY, Zhang Y, Lee DH, Jiang SS, Zhao XN, Zhou JY. Accelerating chemical exchange saturation transfer (CEST) MRI by combining compressed sensing and sensitivity encoding techniques. *Magn Reson Med*. 2017;77:779-786.
32. Glang F, Deshmane A, Prokudin S, et al. DeepCEST 3T: Robust MRI parameter determination and uncertainty quantification with neural networks—application to CEST imaging of the human brain at 3T. *Magn Reson Med*. 2020;84:450-466.
33. Ciet P, Serra G, Bertolo S, et al. Assessment of CF lung disease using motion corrected PROPELLER MRI: a comparison with CT. *Eur Radiol*. 2016;26:780-787.
34. Meier-Schroers M, Kukuk G, Homsi R, Skowasch D, Schild HH, Thomas D. MRI of the lung using the PROPELLER technique: artifact reduction, better image quality and improved nodule detection. *Eur J Radiol*. 2016;85:707-713.
35. Norbeck O, Avventi E, Engstrom M, Engstrom M, Ryden H, Skare S. Simultaneous multi-slice combined with PROPELLER. *Magn Reson Med*. 2018;80:496-506.
36. Henkelman RM, Stanisz GJ, Graham SJ. Magnetization transfer in MRI: a review. *NMR Biomed*. 2001;14:57-64.
37. Jones CK, Huang A, Xu J, et al. Nuclear Overhauser enhancement (NOE) imaging in the human brain at 7 T. *NeuroImage*. 2013;77:114-124.
38. Scheidegger R, Vinogradov E, Alsop DC. Amide proton transfer imaging with improved robustness to magnetic field inhomogeneity and magnetization transfer asymmetry using saturation with frequency alternating RF irradiation. *Magn Reson Med*. 2011;66:1275-1285.
39. Sun PZ, Farrar CT, Sorensen AG. Correction for artifacts induced by B_0 and B_1 field inhomogeneities in pH-sensitive chemical exchange saturation transfer (CEST) imaging. *Magn Reson Med*. 2007;58:1207-1215.
40. Zu Z, Xu J, Li H, et al. Imaging amide proton transfer and nuclear Overhauser enhancement using chemical exchange rotation transfer (CERT). *Magn Reson Med*. 2014;72:471-476.
41. Zaiss M, Zu Z, Xu J, et al. A combined analytical solution for chemical exchange saturation transfer and semi-solid magnetization transfer. *NMR Biomed*. 2015;28:217-230.
42. Zaiss M, Windschuh J, Paech D, et al. Relaxation-compensated CEST-MRI of the human brain at 7 T: unbiased insight into NOE and amide signal changes in human glioblastoma. *NeuroImage*. 2015;112:180-188.
43. Cai KJ, Singh A, Poptani H, et al. CEST signal at 2 ppm (CEST@2ppm) from Z-spectral fitting correlates with creatine distribution in brain tumor. *NMR Biomed*. 2015;28:1-8.
44. Zhang JX, Zhu WZ, Tain RW, Zhou XJ, Cai KJ. Improved differentiation of low-grade and high-grade gliomas and detection of tumor proliferation using APT contrast fitted from Z-spectrum. *Mol Imaging Biol*. 2018;20:623-631.
45. Kim M, Gillen J, Landman BA, Zhou JY, van Zijl PCM. Water sturation shift referencing (WASSR) for chemical exchange saturation transfer (CEST) experiments. *Magn Reson Med*. 2009;61:1441-1450.
46. Desmond KL, Moosvi F, Stanisz GJ. Mapping of amide, amine, and aliphatic peaks in the CEST spectra of murine xenografts at 7 T. *Magn Reson Med*. 2014;71:1841-1853.
47. Heo HY, Zhang Y, Jiang SS, Lee DH, Zhou JY. Quantitative assessment of amide proton transfer (APT) and nuclear Overhauser enhancement (NOE) imaging with extrapolated semisolid magnetization transfer reference (EMR) signals: II. Comparison of three EMR models and application to human brain glioma at 3 Tesla. *Magn Reson Med*. 2016;75:1630-1639.

48. Cai CB, Wang C, Zeng YQ, et al. Single-shot T_2 mapping using overlapping-echo detachment planar imaging and a deep convolutional neural network. *Magn Reson Med*. 2018;80:2202-2214.
49. Ronneberger O, Fischer P, Brox T. U-Net: convolutional networks for biomedical image segmentation. In: Proceedings of International Conference on Medical Image Computing and Computer-Assisted Intervention (MICCAI), Munich, Germany; 2015:234-241.
50. Ledig C, Theis L, Huszar F, et al. Photo-realistic single image super-resolution using a generative adversarial network. In: Proceedings of IEEE/CVF Conference on Computer Vision and Pattern Recognition (CVPR), Honolulu, HI; 2017:105-114.
51. Nie D, Trullo R, Lian J, et al. Medical image synthesis with deep convolutional adversarial networks. *IEEE Trans Biomed Eng*. 2018;65:2720-2730.
52. Roussel T, Rosenberg JT, Grant SC, Frydman L. Brain investigations of rodent disease models by chemical exchange saturation transfer at 21.1T. *NMR Biomed*. 2018;31:e3995.
53. Chen L, Zeng HF, Xu X, et al. Investigation of the contribution of total creatine to the CEST Z-spectrum of brain using a knockout mouse model. *NMR Biomed*. 2017;30:e3834.
54. Chen L, Barker PB, Weiss RG, van Zijl PCM, Xu JD. Creatine and phosphocreatine mapping of mouse skeletal muscle by a polynomial and Lorentzian line-shape fitting CEST method. *Magn Reson Med*. 2019;81:69-78.
55. Zaiss M, Deshmane A, Schuppert M, et al. DeepCEST: 9.4 T chemical exchange saturation transfer MRI contrast predicted from 3 T data—a proof of concept study. *Magn Reson Med*. 2019;81:3901-3914.
56. Zhang J, Wu J, Chen SJ, et al. Robust single-shot T_2 mapping via multiple overlapping-echo acquisition and deep neural network. *IEEE Trans Med Imaging*. 2019;38:1801-1811.
57. Zaiss M, Ehses P, Scheffler K. Snapshot-CEST: optimizing spiral-centric-reordered gradient echo acquisition for fast and robust 3D CEST MRI at 9.4T. *NMR Biomed*. 2018;31:e3879.

SUPPORTING INFORMATION

Additional Supporting Information may be found online in the Supporting Information section.

FIGURE S1 Flow chart of synthesized sample generation under a series of saturation frequency offsets

FIGURE S2 Results reconstructed from the networks with different loss functions. A, F, K, Reference images. B, G, L, Results reconstructed from the network with GDL term in the loss function. E, H, M, Results reconstructed from the network without GDL term in the loss function. D, I, N, Different maps between (A, F, K) and (B, G, L). E, J, O, Different maps between (A, F, K) and (C, H, M)

How to cite this article: Guo C, Wu J, Rosenberg JT, Roussel T, Cai S, Cai C. Fast chemical exchange saturation transfer imaging based on PROPELLER acquisition and deep neural network reconstruction. *Magn Reson Med*. 2020;84:3192–3205. https://doi.org/10.1002/mrm.28376